

UC Davis

UC Davis Previously Published Works

Title

Adaptive optics scanning laser ophthalmoscopy and optical coherence tomography (AO-SLO-OCT) system for in vivo mouse retina imaging.

Permalink

<https://escholarship.org/uc/item/24k2d1w6>

Journal

Biomedical Optics Express, 14(1)

ISSN

2156-7085

Authors

Zhang, Pengfei
Wahl, Daniel J
Mocci, Jacopo
[et al.](#)

Publication Date

2023



DOI

10.1364/boe.473447

Peer reviewed



Adaptive optics scanning laser ophthalmoscopy and optical coherence tomography (AO-SLO-OCT) system for *in vivo* mouse retina imaging

PENGFEEI ZHANG,^{1,2}  DANIEL J. WAHL,³ JACOPO MOCCI,⁴  ERIC B. MILLER,⁵ STEFANO BONORA,⁶ MARINKO V. SARUNIC,^{3,7,8} AND ROBERT J. ZAWADZKI^{2,9,*} 

¹School of Optoelectronic Engineering and Instrumentation Science, Dalian University of Technology, Dalian, China

²UC Davis EyePod Small Animals Ocular Imaging Laboratory, Department of Cell Biology and Human Anatomy, University of California Davis, Davis, CA 95616, USA

³Engineering Science, Simon Fraser University, Burnaby BC, V5A 1S6, Canada

⁴Dynamic Optics srl, Piazza Zanellato 5, 35131, Padova, Italy

⁵Center for Neuroscience, University of California, Davis, CA 95616, USA

⁶CNR-Institute for Photonics and Nanotechnology, Via Trasea 7, 35131, Padova, Italy

⁷Medical Physics and Biomedical Engineering, University College London, United Kingdom

⁸Institute of Ophthalmology, University College London, United Kingdom

⁹UC Davis Eye Center, Dept. of Ophthalmology & Vision Science, University of California Davis, 4860 Y Street, Suite 2400, Sacramento, California 95817, USA

*rjzawadzki@ucdavis.edu

Abstract: Optical coherence tomography (OCT) and scanning laser ophthalmoscopy (SLO) are imaging technologies invented in the 1980s that have revolutionized the field of *in vivo* retinal diagnostics and are now commonly used in ophthalmology clinics as well as in vision science research. Adaptive optics (AO) technology enables high-fidelity correction of ocular aberrations, resulting in improved resolution and sensitivity for both SLO and OCT systems. The potential of gathering multi-modal cellular-resolution information in a single instrument is of great interest to the ophthalmic imaging community. Although similar instruments have been developed for imaging the human retina, developing such a system for mice will benefit basic science research and should help with further dissemination of AO technology. Here, we present our work integrating OCT into an existing mouse retinal AO-SLO system, resulting in a multi-modal AO-enhanced imaging system of the living mouse eye. The new system allows either independent or simultaneous data acquisition of AO-SLO and AO-OCT, depending on the requirements of specific scientific experiments. The system allows a data acquisition speed of 200 kHz A-scans/pixel rate for OCT and SLO, respectively. It offers $\sim 6 \mu\text{m}$ axial resolution for AO-OCT and a $\sim 1 \mu\text{m}$ lateral resolution for AO-SLO-OCT imaging.

© 2022 Optica Publishing Group under the terms of the [Optica Open Access Publishing Agreement](#)

1. Introduction

The mouse retina is an important model in vision science and ophthalmic research. Additionally, due to the retina being an optically accessible extension of the brain, mouse models afford the unique opportunity to non-invasively visualize changes associated with neurodegenerative disorders and vascular alterations of neural tissue during the normal progression of the disease as well as during the testing of novel therapeutic strategies. Scanning Laser Ophthalmoscopy (SLO) [1–3] and Optical Coherence Tomography (OCT) [4–9] are two common *in vivo* retinal imaging modalities that have been successfully applied to monitor structural changes in the

retina of living animals, enabling experiments that map changes in retinal morphology and its optical properties (scattering, intrinsic and extrinsic fluorescence) over seconds, days, weeks and months. The combination of these modalities provides a wealth of complementary information, as demonstrated by our previous work [10–13] and the work of other groups [14–18].

Most retinal imaging systems employ the eye's natural optics as the imaging objective. Due to optical aberrations of the lens and cornea, it is impossible to use the full pupil of the eye while maintaining diffraction-limited performance. Consequently, both SLO and OCT typically use imaging beams whose width is a small fraction of the eye's pupil diameter [19,20]. As a result, both systems offer a relatively low lateral resolution of the retina. However, high-resolution imaging is required to visualize the cellular structures and allow studies of the cellular-level processes in the living retina. A hardware-based AO improves the system's optical performance by compensating for the ocular aberrations using wavefront shaping components (deformable mirror or spatial light modulators), allowing the use of the maximum available numerical aperture of the imaging objective (in our case, mouse eye), and thus the maximum available lateral resolution [21–25], as demonstrated by several groups [26–31]. Recent developments of two-photon fluorescence-based mouse retinal AO-SLOs also showcase the importance of the AO technology in basic science research [32–34].

Here we report our work on integrating OCT into our previously reported AO-SLO system [35] for *in vivo* mouse retina imaging. The manuscript was organized as follows: first, the description of the system design is provided; then, the OCT performance is given by measurements of its sensitivity roll-off and its axial resolution. Further, the AO-SLO-OCT simultaneous acquisition is demonstrated on a model eye. Next, a mouse retina was imaged with AO-SLO and with AO-OCT to show the high control of the AO axial focus position, thanks to highly axially localized enhancement in retinal reflectivity. Finally, several critical aspects of system construction are discussed, followed by a brief conclusion.

2. Materials and methods

2.1. System description

In our previous report, an *in vivo* mouse retinal AO-SLO imaging system was built and successfully applied to study cellular morphology *in vivo* [35]. Before the addition of an OCT channel, the Shack-Hartmann wavefront sensor (SHWS) [36] and the AO controller were upgraded to a new version that can measure and correct aberrations at 100+ Hz using high spatial sampling of the pupil (40×40 lenslets on 2×2 mm² pupil). Figure 1 shows changes introduced to the AO-SLO system to allow its integration with OCT detection resulting in the AO-SLO-OCT instrument. These included:

- (1) The light for wavefront sensing and SLO imaging was introduced into the system by beamsplitter BS1, then the light passed through a cascade of 4f telescopes (all spherical mirrors except the last lens) into the mouse eye, ensuring optical conjugation of the mouse pupil with the Deformable Mirror, the X- and Y-Scanners, Imaging objective lens, and SH-WFS lenslet array.
- (2) A short-pass ultra-flat dichroic mirror (D3, t750spxr-xt-uf, Chroma) was used to introduce OCT light into the AO-SLO system, which also acts as the sample arm of the AO-OCT system.
- (3) A separate reference arm matching the path lengths of the AO-OCT sample arm (~11.5 meters long) was built and included D1 to match the dispersion of both arms.
- (4) A supercontinuum laser (NKT) served as the OCT light source. The OCT light was centered at 800 nm with 65 nm FWHM bandwidth, which provided about 6.3 μ m axial resolution in air.

- (5) A spectrometer comprising of 1200 lines/mm diffraction grating (Wasatch Photonics 1200lpmm at 840 nm), a 4096 pixels line scan camera (Basler SPL4096-140 km), and imaging optics was built in-house. The OCT system offered a 200 kHz A-scan rate for 1024 pixels acquired by the Basler line scan camera.

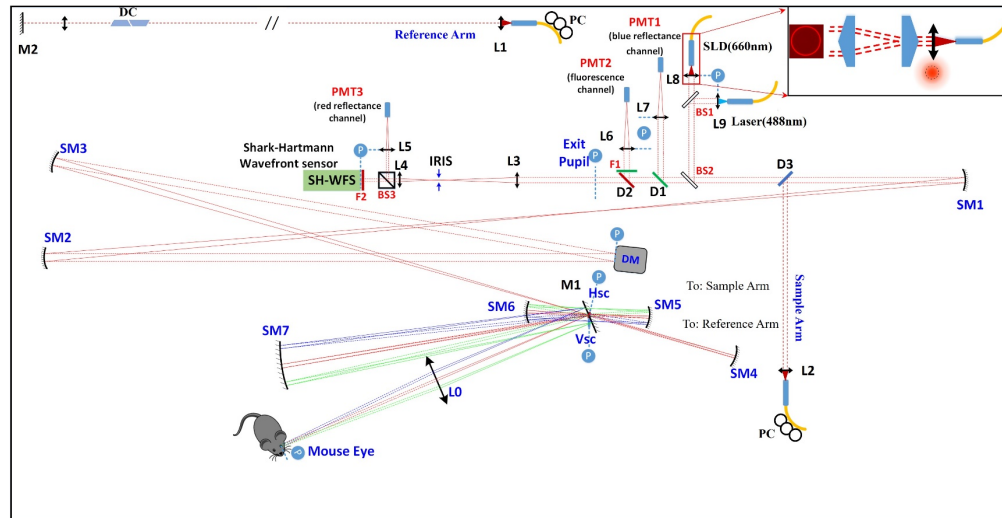


Fig. 1. Schematic of the multi-modal AO-SLO-OCT mouse retinal imaging system: BS# - beam splitter; DC - dispersion compensation; D# - dichroic mirror; DM - deformable mirror; PMT - photomultiplier tube; P (circled in blue and marked with blue dashed line) - optical planes conjugate with the pupil; SLD - superluminescent diode; SM# - spherical mirror, M# - mirrors, L# lens, Hsc/Vsc - horizontal/vertical scanner. Insert in the top right corner visualizes the fiber launch of the AO beacon implementing the pair of optical axicons (resulting in ring illumination).

The Shack-Hartmann wavefront sensor-based AO systems are usually very sensitive to back-reflections from the optical elements. In our current system, there is a strong back-reflection from the last lens (L0 in Fig. 1), as well as from the contact lens and mouse cornea. To eliminate these reflections, in our previous AO-SLO system, a small aperture stop (~ 2 mm in diameter) was placed immediately after the collimator of the SLD light source to create a ring illumination for the beam used for wavefront sensing. As an alternative approach, here we tested an axicon lens pair (25.4 mm in diameter, 20° angle, 10 mm axial separation, Asphericon Inc. Sarasota, USA) to create annular/circular collimated illumination light, as shown in the top right corner in Fig. 1. The axicon lens pair converts the Gaussian beam profile into a Bessel beam. The ring diameter is adjusted by moving the axial position of the second axicon. This configuration also allows the reduction of spherical aberration and extension of the depth of focus of the wavefront beacon. However, it may introduce additional aberration if not correctly aligned (as will be further described in the Discussion).

The resulting AO-SLO-OCT system has a 2 mm beam size at the mouse pupil, which is equivalent to a numerical aperture (NA) of ~ 0.5 [37] and could provide lateral and axial resolution of AO-SLO $1\times$ and $8\times$ of the imaging wavelength according to the Abbe's diffraction formula for lateral ($0.5\lambda/NA$) and axial ($2\lambda/NA^2$) resolution, respectively. The imaging power is $100\ \mu\text{W}$ for SLO and wavefront sensing together and $600\ \mu\text{W}$ for the OCT beam.

2.2. Animal handling

The animal handling in this work was performed in accordance with the guidelines of the animal study protocol approved by the University of California Animal Care and Use Committee (IACUC). Pigmented (C57Bl/6) mice from Jackson Labs (2-6 months old, females) were used in the experiments. During imaging, the mice were anesthetized with isoflurane (2% in O_2), and the eye was dilated with tropicamide (1%) and phenylephrine (2.5%). The anesthetized mouse was aligned to a zero Diopter contact lens (Unicon Corporation, Osaka, Japan) with a gel (GenTeal, Alcon, Fort Worth, United States) placed between the lens and the cornea to prevent dehydration and the development of cataracts.

3. Results

3.1. Sensitivity roll-off and axial resolution of the OCT sub-system

The spectrum of the light source was measured by our custom build spectrometer. As shown in Fig. 2 (a), it had a ~ 65 nm FWHM bandwidth. The spectrometer mapping of pixels to wavenumbers (spectral mapping) was calibrated, as shown in Fig. 2 (b). Then, we measured spectrometer sensitivity roll-off by placing a sample mirror at different depths, as shown in Fig. 2 (c). Figure 2 (d) shows the FWHM axial resolution at different depths. The average resolution within the 1 mm range from the zero path length difference is about $6.3 \mu\text{m}$ in air, which translates to about $4.7 \mu\text{m}$ in tissue, assuming a tissue refractive index of 1.34.

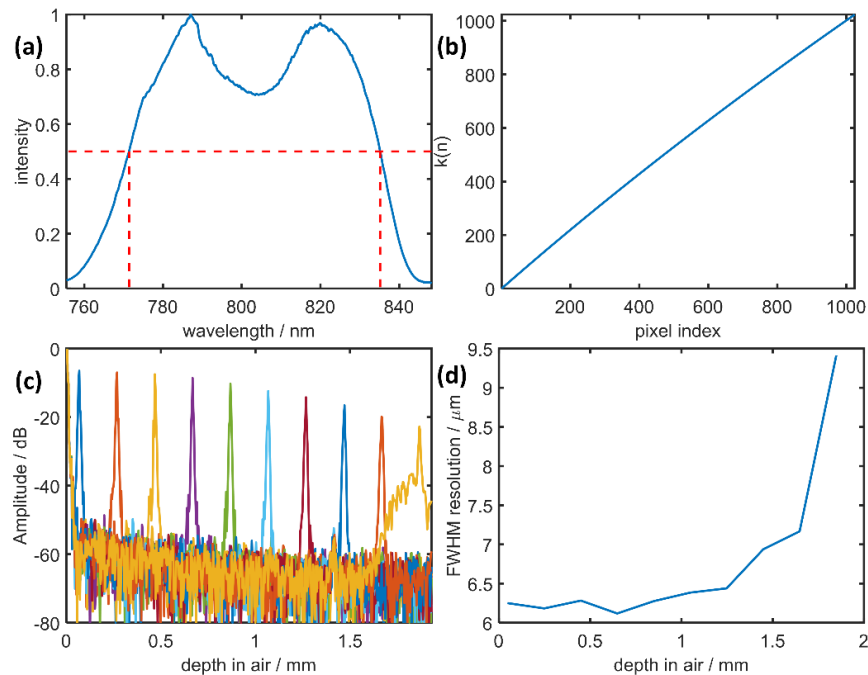


Fig. 2. OCT spectrometer calibration. (a): normalized reference arm spectrum measured by the custom spectrometer; (b): spectral mapping of the spectrometer: wavenumber $k(n)$ versus pixel index; (c): Sensitivity roll-off as a function of depth; (d): FWHM resolution at different depths.

3.2. AO-SLO-OCT imaging of a model eye

First, a model eye with a 100 mm focal length achromatic lens as the objective and a paper with printed text as the retina was used to test our combined AO-SLO-OCT system. The SLO and OCT images were acquired simultaneously. The images of SLO, OCT en face projection, and OCT B-scans before and after AO correction are shown in Fig. 3 (a), which clearly showcases the overall enhancement of AO in terms of image intensity. The OCT en face intensity projection is also shown to visualize improvement in image sharpness after AO correction. We quantified the improvement in image quality by comparing changes in wavefront RMS error (Fig. 3 (b) from 0.3 μm to 0.03 μm), as well as the intensity histogram changes (Fig. 3 (c) and (d) for SLO and OCT en face projection, respectively). Figure 3 (e) shows the OCT A-line profile changes (averaged from 50 A-scans centered at B-scan shown in Fig. 3 (a)). The OCT A-scan line intensity profile (linear to the sample arm light amplitude) increases about 2.3 times after AO correction. Note that the images before AO correction for the model eye (Fig. 3) were collected with a ‘flat’ deformable mirror, thus without correcting system residual aberration. This is because, due to minimal aberrations of the model eye, a very moderate improvement would be observed when correcting model eye aberrations only. This correction of the system aberrations was used as a non-AO DM setting when imaging the mouse retina (Fig. 5,6 & 9). The images before AO correction were collected while residual system aberrations were corrected. Thus, the images before and after AO correction for mouse eyes are comparing the images with only system aberration corrected (before AO correction) and with full AO correction of both system and mouse ocular aberrations (after AO correction).

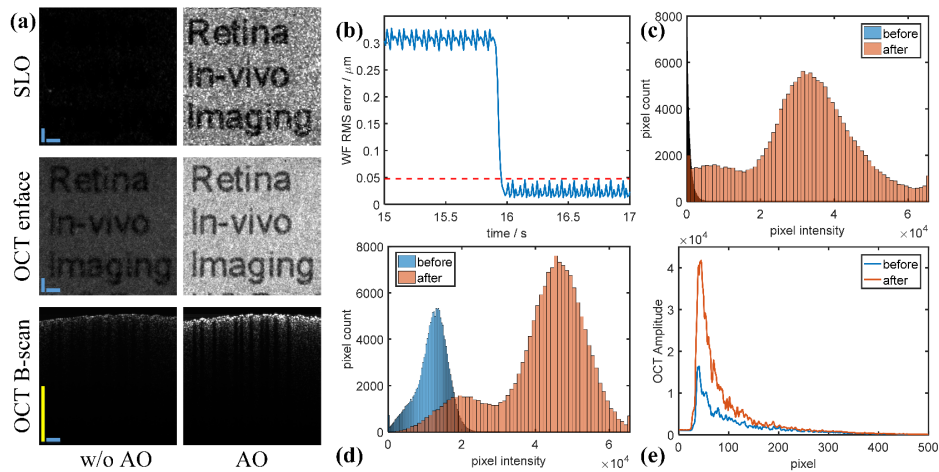


Fig. 3. Example images acquired on a model eye with SLO and OCT without/with adaptive optics and its analysis. (a) SLO and OCT images without (left) and with (right) AO, (b) Wavefront RMS error changes, (c) SLO image histogram, and (d) OCT en face projection histogram change. (e) OCT line intensity profile changes before and after AO correction for the images shown in panel (a). Scale bar: 100 μm (yellow), 1 mm (blue).

Note that the improvement of the OCT signal seems smaller than the SLO signal in Fig. 3. This is due to the use of arbitrary dynamic range to display both data, making a direct comparison of the increase in intensity not possible. Namely, there are two thresholds (minimum and maximum) for the SLO signal voltage, the voltage below the minimum is digitized to be zero, and the voltage above the maximum is digitized to be $2^{16}-1$, otherwise to an unsigned 16-bit number. Depending on the setting of the SLO minimum threshold, we can arbitrarily change the perceived increase in brightness. In our SLO voltage threshold setting, we tend to set it, so the image before AO

correction is close to zero intensity (dark) so that there is a more dynamic range for the signal after AO correction. We do not actively adjust the dynamic range of the OCT images. Thus, the improvement in the SLO signal appears to be much better than for the OCT signal.

3.3. AO-SLO and AO-OCT imaging of a living mouse retina

The performance of the AO-SLO sub-system was reported in our previous publications [35,38–40]. The AO-SLO data acquisition was running alone at a 10 Hz frame rate and 1° FOV ($\sim 36 \mu\text{m} \times 36 \mu\text{m}$). Overall, it demonstrated good quality in imaging the relatively large structures and fluorescently labeled cells in the mouse retina. However, photoreceptor imaging was still very challenging due to the small size of rods (the dominant photoreceptor class in rodent retinas). The first demonstration of successful imaging of the mouse rod photoreceptors mosaic in our system was reported in [38], here, the data is revisited, as shown in Fig. 4.

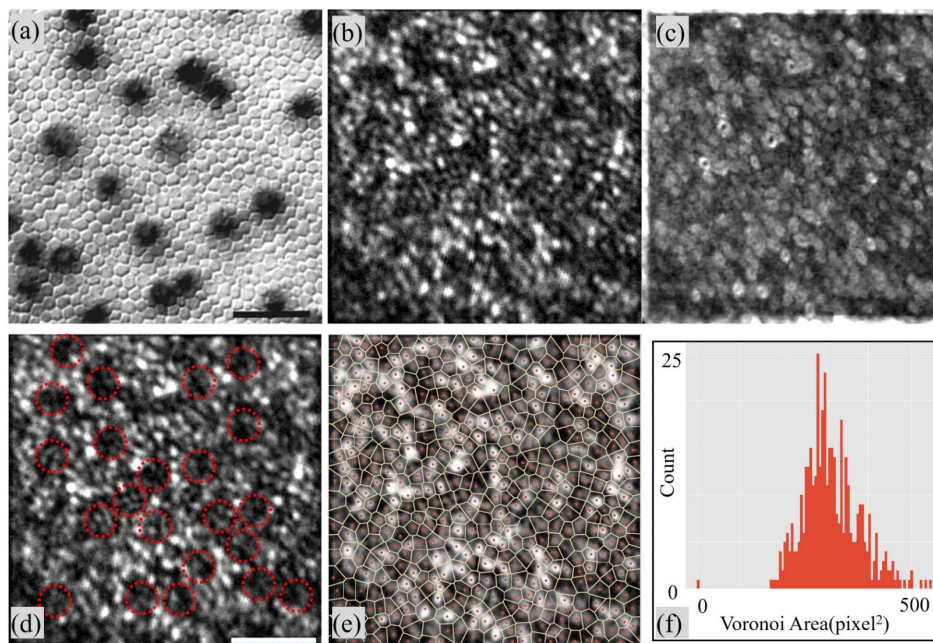


Fig. 4. AO-SLO imaging of the mouse photoreceptors: (a) The mosaic of inner segments of rods (lighter, polygonal structures) and cones (dark regions) from a DIC microscopic image [41], (b) 663 nm AO-SLO reflectance photoreceptor mosaic image, averaged from 100 registered raw images (see Visualization 1), (c) standard deviation projection from the same 100 raw images, (d) the potential cones manually marked by the red circles corresponding to the dark regions in the mosaic. (e) Jeon Voronoi tessellation of the photoreceptors in panel (b), (f) Histogram Jeon Voronoi elements size in (e). Scale bar: 10 μm .

Figure 4 (a) shows the DIC (Differential Interference Contrast) microscopic imaging of the mouse photoreceptor inner segments with only rods visible as light polygonal shapes while cones are invisible (dark regions) [41]; in the averaged intensity image from our AO-SLO system, bright dots are visible with a high variance in the intensity (Fig. 4 (b)), these were attributed to rods given the size and spacing similar to the rods mosaic ($\sim 1.6 \mu\text{m}$ in diameter) [38]. Here we found that the standard deviation projection of the same data generated a mosaic image with higher contrast which has some similarities to the rod's polygonal shape shown in Fig. 4 (a). (Figure 4 (c)) [42]; In Fig. 4 (b-c), as observed previously, the standard deviation projection provides much better contrast than the averaged intensity image. We think that it is due to the residual

eye motion artifact still being present after registration. Thus, there is always misalignment between frames. Therefore, standard deviation projection provides an increased signal at the edges of the cells, which makes the cells more visible, however, at the price of increasing their size and distorting the mosaic. This application of standard deviation for image enhancement has been previously reported by Yao et al. [42]. However, cones are not visible in these images. Two more examples comparing median averaging and standard deviation averaging of mouse photoreceptor mosaic is shown in Fig. S1 in the supplement. The example videos of registered raw AO-SLO images of photoreceptor mosaic acquired in five different mice have also been included: (see [Visualization 1](#); [Visualization 2](#); [Visualization 3](#); [Visualization 4](#); [Visualization 5](#)). When comparing panels (a) and (b) in Fig. 4, we manually picked some dark regions marked by the red circles as the potential positions for cones (possibly less reflecting in mice), as shown in Fig. 4 (d). Nevertheless, it is very interesting why cones in the mouse retina do not produce a strong dominating reflection like the cones observed in other species, including humans and non-human primates. Interestingly, the strong reflection of cones, compared to the relatively weak rod reflections, allows imaging of the human photoreceptor mosaic in the periphery without adaptive optics. The Jeon Voronoi tessellation of the photoreceptor mosaic was performed, and the histogram of the areas of Voronoi elements was calculated, as shown in Fig. 4 (e) and (f), respectively. There were 501 rods and 22 cones in total with an average area of Voronoi element of 318 pixel^2 , corresponding to $3.18 \mu\text{m}^2$. The estimates of cell densities are 365,960 and 16,070 cells/ mm^2 for rods and cones, respectively. Both values are close to the numbers reported in [43], which are 437,000 and 12,400. The difference could be due to photoreceptor diameter dependence on eccentricity. Assuming a hexagonal shape of Voronoi elements and the observation that Voronoi elements overestimate the area of photoreceptors by about 60% (see Fig. 4 (e)), the average diameter of the rod is calculated at $1.6 \mu\text{m}$, which matches the reported diameter of mouse rods ($1.6 \mu\text{m}$ in [22], $1.4 \mu\text{m}$ in [43]). To further showcase the performance of our AO-SLO system Fig S2 in the supplement shows examples of AO-SLO large-field of view imaging with the 488 nm reflectance channel with an imaging focus set at the retina nerve fiber layer (RNFL) Fig. S2 (a), with the corresponding fluorescence angiography image in Fig. S2 (b). Additionally the example results of AO-SLO imaging with the 663 nm reflectance and focus set on the RNFL are shown in Fig. S2 (c-d).

The performance of the AO-OCT sub-system was tested by in vivo imaging of the retina of a pigmented mouse. The AO-OCT data acquisition was running alone at 200kHz A-scan rate and 6° FOV ($\sim 216 \mu\text{m} \times 216 \mu\text{m}$). Due to the chromatic aberration, the AO-OCT beam (centered at 800 nm) was naturally focused deeper in the retina, in the choroid, as shown in Fig. 5 (a). Only RPE and choroid layers are visible in the AO-OCT B-scans (presented on a linear intensity scale) before AO correction. After closing the AO loop, the A-scan intensity profiles (averaged from the center 100 A-scans from each B-scan) clearly show the signal enhancement around RPE-choroid layers, while the rest of the retinal layers are not enhanced. To visualize other layers, we needed to axially shift the OCT focus to the layer of interest. Note that the AO-OCT focal plane can be adjusted independently from the AO focus when the OCT sample arm fiber tip position is moved axially with respect to the collimating lens. This will shift the OCT focal plane while the AO focus remains fixed during this process because the wavefront sensing path, including the AO beacon, deformable mirror, and relay lens pairs are unchanged. Actually, there are two ways to shift this focus plane in our system, one is by adding defocus to the deformable mirror after “freezing” AO correction, and the other way is to move the OCT sample arm fiber tip position further from the collimating lens (changing divergence of the OCT beam at the system entrance). Here we tested the second way, as demonstrated in Fig. 5. During the entire progressive focus series in Fig. 5, 26 different focus positions were tested without and with AO correction, so 52 datasets were collected. The whole process took ~ 27 mins. It is worth noting that: when the light focuses on IS/OS layer, there is an additional reflection that appears in the axial intensity

profile, as shown in Fig. 5 (c), which might correspond to cone outer segment tips; when the light focus on ONL layer (Fig. 5 (g)), it becomes more visible than adjacent plexiform layers which are not seen in standard OCT images. It was noted that the OCT signal of OPL and INL dropped significantly after AO correction in Fig. 5 (e-f). Considering the focus for wavefront sensing is fixed during the axial scanning of OCT focus, the decrease of OCT signal is attributed to the improvement of the depth of focus of AO corrected OCT beam. Additionally, it has been reported that aberrations could substantially change with axial depth in the mouse eye, and the AO correction performance could be compromised if the wavefront sensing position is shifted away from the imaging plane [34,44]. Thus, the performance of the axial scanning of the OCT focus might depend on the reference focal plane position for AO correction.

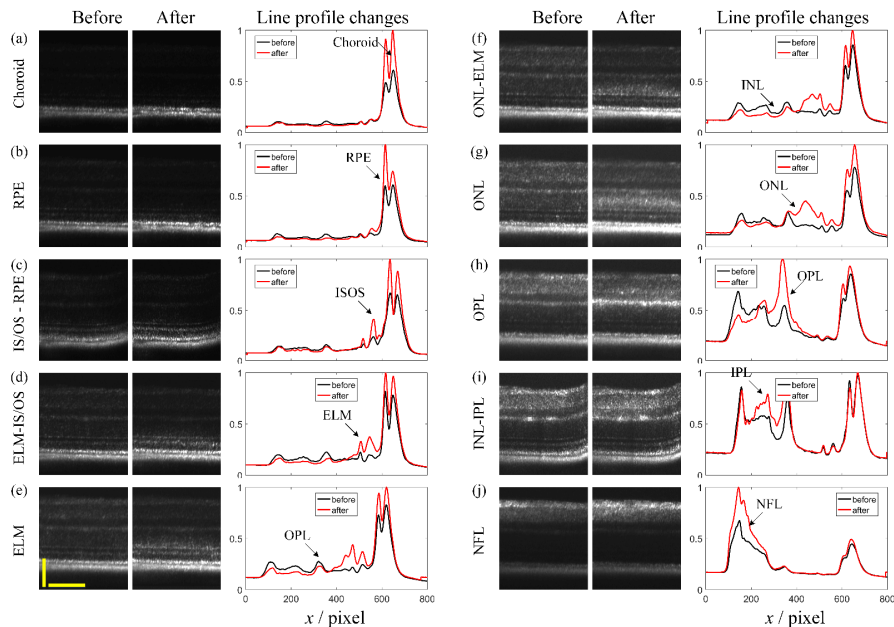


Fig. 5. *In vivo* mouse retinal AO-OCT B-scan images showing the localization of the focal plane in our AO-OCT system. The B-scans show the improvement in image intensity only within a very limited depth after AO correction due to the relatively high NA of the mouse eye and corresponding confocal depth of focus; the line profile changes show the OCT signal changes (proportional to the sample light amplitude). RPE: retinal pigment epithelium; IS/OS: inner segment /outer segment of photoreceptors; ELM: external limiting membrane; ONL: outer nuclear layer; OPL: outer plexiform layer; IPL: inner plexiform layer; INL: inner nuclear layer; NFL: nerve fiber layer. Scale bar: 100 μm . Line profiles scaling factor (0.5 $\mu\text{m}/\text{pixel}$).

We further made the maximum projection on the datasets with a shifting focus at 25 different locations distributed across the retina (gray lines in Fig. 6(a)). Because the ELM peak appears at all the line profiles, it was used to align the OCT line profiles axially. The result without AO was shown by the black line, while the result with adaptive optics was shown by the red line. It can be seen that adaptive optics can increase the OCT signal intensity at almost every location. The ratio between the OCT signal with and without adaptive optics was calculated and shown in Fig. 6 (b), with a median value of 1.40. Note that the apparent shift of the NFL peak could represent the signal enhancement of the cells (e.g., macrophages) closing to the inner limiting membrane in the vitreous humor. Overall, this suggests that a dynamic focus would be needed to

fully utilize the advantage of AO to image all the layers of the mouse retina. This could be done by the introduction of a variable focus lens or other mechanical focus-shifting techniques [45].

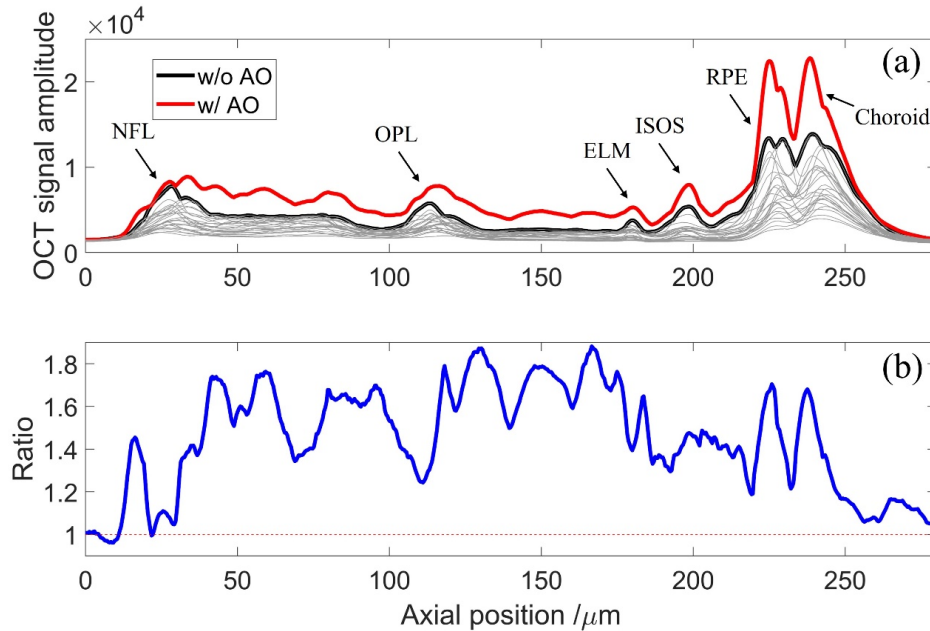


Fig. 6. The line profile intensity comparison before (black) and after (red) AO close loop correction for all retinal layers, (a) the maximum retinal reflectivity from 25 line profiles (grey) with different OCT focus planes, (b) the ratio between the maximum layer reflectivity with AO correction and without AO correction. 1.6-1.8 times improvement could be achieved for highly reflecting retinal layers.

4. Discussion

4.1. Dispersion compensation for the broadband light source in AO-SLO-OCT

One of the complications we encountered during the AO-SLO-OCT system development was the dispersion compensation of the OCT signal for the broadband light source. In most OCT systems, the differences in dispersion between the sample and reference arm are usually kept to the minimum by using the same thickness of the dispersive materials in the sample and reference arm (hardware dispersion compensation). Additionally, any unmatched residual dispersion is compensated in OCT signal postprocessing by adding a dispersive phase component to the spectral fringe before Fourier transform [46]. Since OCT was added to our existing AO-SLO system, we introduced the OCT sample beam into the AO-SLO system using reflection by a dichroic mirror (D1), as shown in Fig. 7 (b), instead of the preferred transmission of the OCT beam by a dichroic mirror (D1) (Fig. 7 (a)).

To compensate for the dispersion introduced by the reflection of a dichroic mirror in the sample arm, we used another dichroic mirror in the reference arm. Although two identical ultra-flat dichroic mirrors were used to match the dispersion between the reference arm and sample arm, the residual dispersion couldn't be matched using standard software dispersion compensation: Fig. 7 (c) shows the best corrected PSFs for different bandwidths of OCT light source (The corresponding spectra are shown in Fig. 7 (d)). The PSF from broadband (190 nm bandwidth) light source has a very broad and complex PSF if compared to narrowband (40 nm bandwidth) light source. The theoretical PSFs for each spectral bandwidth are shown for comparison and

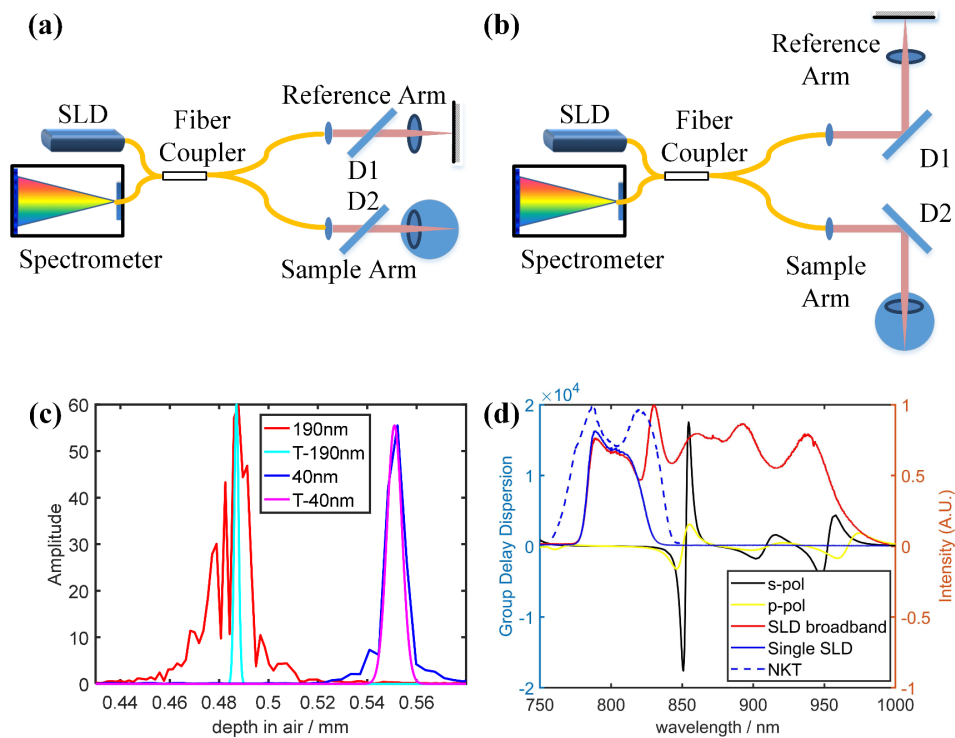


Fig. 7. Group Delay Dispersion introduced by reflection from an ultra-flat dichroic mirror limited the useful spectral range for the OCT sub-system, (a, b) simplified OCT configuration sketch of a preferred use mode of the dichroic and our system (Reflection mode of a dichroic), respectively; (c) Axial PSF for light sources with different bandwidth: 190 nm centered at 870 nm and 40 nm centered at 800 nm, “T-”: Theoretical PSF; (d) group delay dispersion for s- and p-polarized light, the spectrum of the broadband SLD / single SLD and NKT sources, respectively.

marked by “T-”. This illustrates our inability to properly match dispersion in this configuration and what would result in the image artifacts and axial blurring of the OCT images. The reason for this behavior is group delay dispersion (GDD) [47] introduced by the dichroic mirrors. Figure 7 (d) also plots its GDD for s- / p- polarized light, which shows a considerable spike in GDD around 850 nm. This narrowed down the useful bandwidth for our OCT light source. To avoid this GDD anomaly, we decided to limit our light source spectrum from 760 nm to 840 nm (Note that the dichroic is a 750 nm short pass filter). Unfortunately, this lowers the axial resolution of our OCT system. However, due to the limited spectral range, we could run our OCT detection spectrometer two times faster (200 kHz) and limit chromatic aberration’s effect in both transverse and longitudinal directions [48]. We had two light sources that could operate in this spectral range an SLD with 40 nm FWHM spectral bandwidth and an NKT source with a tunable filter. We decided to use the NKT source in our experiments because it can offer ~ 25 nm broader bandwidth of light and three times more power.

4.2. Aberrations introduced by axicon pair

The axicon pair in our system was introduced into the WFS beacon beam to reduce the back-reflection from the mouse cornea/contact lens (by creating the ring intensity illumination profile), without reduction in the beam power. Additionally, this results in creating a Bessel beam on

the retina, which could benefit AO by extending the depth range of focus. We want to point out that while this is a potentially very attractive solution, it is also very sensitive to the proper alignment of axicons. Figure 8 shows two examples of the aberration introduced by the not properly aligned axicon pair, as detected by our wavefront sensor, after applying wavefront sensorless AO correction using the intensity of the image created by the same light [49,50]. This test was performed on the model eye and showcased the need for more detailed studies when Bessel Beams are used as the AO beacons.

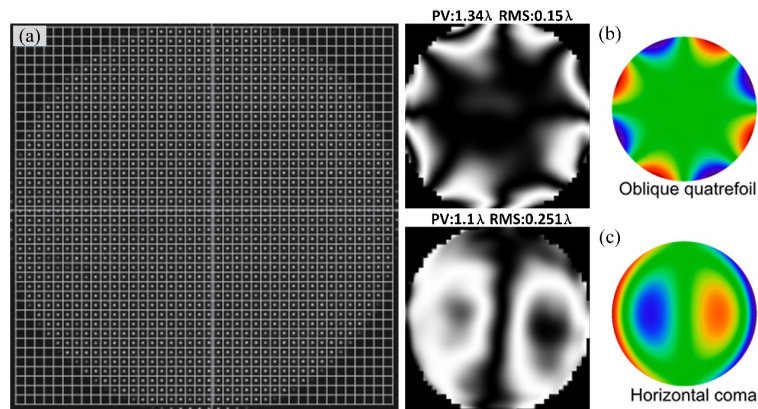


Fig. 8. An image of the HS-WFS spots and two examples of aberrations introduced by the misaligned axicon pair used to generate the AO beacon beam. (a) An exa image of the HS-WFS spots from the model eye; (b) Oblique quatrefoil of RMS 0.15 λ; (c) Horizontal coma of RMS 0.25 λ.

Note that the Hartmann-Shack wavefront sensor measures single-pass aberrations mostly, not the double-pass. Thus, the wavefront sensor does not detect the wavefront of the annular beam passing toward the retina. It measures mostly backscattered light from the AO reference plane. Thus, although the beam passing axicon pairs is of annular shape, the scattered light from the eye fills the whole eye pupil. The aberrations created by the misaligned axicon pair make the AO reference spot blurry, lowering both the resolution and signal intensity, and could also “leak” to our detector due to the presence of back-reflected light. The wavefront sensor could be used as feedback to align the axicon pairs once we confirm what causes those aberrations and how their presence is affected by backscattering vs. back reflections in the model eye.

4.3. Estimation of the AO-OCT system lateral and axial resolution before and after AO correction in the living mouse eye

The smallest axially extended structure in the living mouse eye that can be used to estimate AO-OCT system axial resolution is the external limiting membrane (ELM), or outer limiting membrane (OLM), which is a network of junctional complexes between Müller cells and the photoreceptors they encircle that contributes to barrier functions in the neural retina [51]. The network-like structure (Fig. 9 (a) inset) has a thickness and fine structures which are at the micrometer level, as estimated from the images in [52]. Here we use the intensity line profiles extracted from the averaged retinal AO-OCT B-scan in the lateral and axial direction across the ELM to estimate the lateral and axial resolution of the AO-OCT system. The 100-frame-averaged B-Scans acquired over the 3° FOV before and after AO correction were shown in Fig. 9 (a) and (d), respectively. These two averaged B-scans were aligned via Fiji ImageJ ‘StackReg’ plugin before comparison. A line right on top of ELM was drawn, and the corresponding intensity values were extracted and shown in Fig. 9 (b) for comparison.

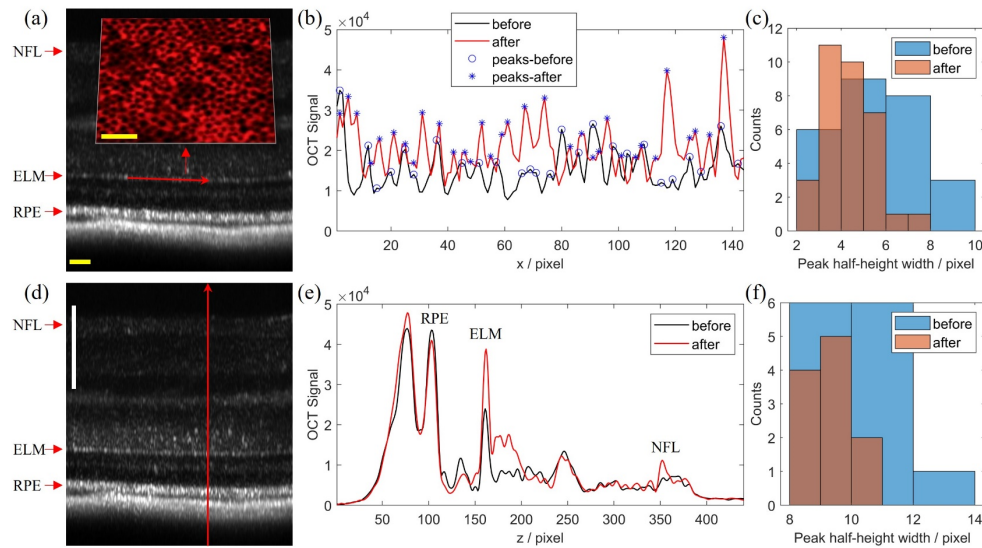


Fig. 9. Estimation of the AO-OCT lateral and axial resolution before and after AO correction in the living mouse eye, (a) the averaged AO-OCT B-scan before AO correction with an inset showing the fluorescence microscopy image of the ELM labeled with glutamine synthetase and occludin in a normal rat. Occludin is located around photoreceptors at the glial membrane and between glial Müller cell structures, (b) the intensity line profile at the ELM (location and direction indicated by the red line in (a)), (c) the histogram of the Full Width at Half-Maximum (FWHM) width of the ELM structures before and after AO corrections, (d) the averaged AO-OCT B-scan after AO correction, (e) a pair of representative line profiles (location and direction indicated by the red line in (d)), (f) the histogram of the ELM band FWHM width before and after AO correction. Scale bars: 100 μm (white), 10 μm (yellow).

It can be seen that there is an increase in contrast and that the lateral features in this line appear narrower. Note that due to the B-Scan averaging, these features possibly represent the true microstructure of the ELM rather than the speckle field. With Matlab ‘findpeaks’ function, the peaks and their Full Width at Half Maximum (FWHM) were extracted, and the FWHM histograms were shown in Fig. 9 (c). The numbers of peaks before and after AO correction were 26 and 33, respectively. The averaged FWHMs were 5.10 and 3.97 pixels, which is $\sim 1.38 \mu\text{m}$ and $\sim 1.07 \mu\text{m}$. Two representative A-scans before and after AO correction were shown in Fig. 9 (e), which shows the OCT focus in the lower part of ONL close to ELM. Nevertheless, ELM signal amplitude increased $\sim 2\times$ after AO correction. 11 and 13 ELM peaks with clear gaussian distribution were extracted and processed with Matlab ‘findpeaks’ function. The histogram of the FWHM was shown in Fig. 9 (f) with average values of 10.59 and 9.43 pixels, which is $\sim 7.2 \mu\text{m}$ and $\sim 6.4 \mu\text{m}$. Given the weight (w) is the PSF convoluted with the size (L) of the structures, which has a theoretical relationship of $w^2 = PSF^2 + L^2$, and the exact number of L is unknown, the accurate PSF cannot be recovered this way. However, it still provides an estimation of the resolution to some extent, which reflects the expectation that AO improves mainly the lateral resolution for the OCT system.

4.4. Technical challenges associated with AO-SLO-OCT imaging of mouse retina

The success rate of visualizing photoreceptor mosaics in multiple mice with AO-SLO was close to 100% over several animals imaged. We achieve that by focusing our AO correction on the individual scattering spots (photoreceptors) visible in real-time in the raw image during

acquisition. We achieve that despite multiple challenges associated with the implementation of AO in the small mouse eye. However, we consistently observed that a considerable amount of motion artifacts were present in the acquired data mostly due to the high magnification of the AO system (5-10 \times higher than in *our* mouse [53] or clinical AO retinal *imaging* systems [27]), which could not be corrected in postprocessing for AO-OCT data with the method currently used in our laboratory (supplementary material). The limited acquisition speed of our current AO-OCT system amplified this issue. For example, to get the AO-SLO photoreceptor images shown in Fig. 4, the SLO frame rate was 10 Hz with 1 $^\circ$ FOV ($\sim 36\ \mu\text{m} \times 36\ \mu\text{m}$, 400×200 pixels with a 2kHz fast-axis sinusoidal scan). However, the AO-OCT volumetric acquisition rate for a similar FOV was about five times slower (raster scan), making further registration and volume averaging for contrast enhancement impossible. Similar to clinical AO-OCT imaging, the speckle contrast present in the individual AO-OCT volumes is too high to visualize cells in *en-face* planes. Thus, the application of AO-OCT demonstrated here is limited, and its high-resolution advantage over traditional non-AO OCT suffers from the currently limited acquisition speed of our OCT system. Additionally, the reduced depth-of-focus of the mouse AO-OCT system makes the 3D registration even harder, especially when the axial shifts of focus and retinal axial position are present during mouse breathing. We believe that improvements in OCT image acquisition speed are critically needed to reduce this problem and to fully highlight the benefits of AO-OCT imaging in the mouse eye. The higher acquisition speeds would also allow for the implementation of a more reliable image registration algorithm and a more accurate chromatic aberration compensation method.

Note that, in the data presented here, the system was acquiring data simultaneously only during the model eye imaging, while each modality ran independently for *in vivo* imaging. This was due to the limitations caused by the current acquisition speed of our OCT engine. For example, to image the photoreceptor mosaic, a small FOV (typically 1 $^\circ$, maximum 2 $^\circ$) is required with a sampling density of 400×200 pixels across the FOV and a frame rate of 10 Hz. Our AO-SLO imaging speed is barely sufficient to allow correction of the eye motion artifacts and success registration between frames. However, based on our experience, a larger FOV (3-6 $^\circ$) is required to get 'good' AO-OCT images due to the presence of speckles and the inability to correct eye motion artifacts to register multiple volumes. This is because the OCT engine volume rate is 5 \times slower than the AO-SLO frame rate. Thus, running the two imaging modalities simultaneously at 200kHz would significantly reduce the performance of AO-SLO in the current configuration. Increasing the OCT volume rate to match the AO-SLO frame rate is needed to improve the utility of our combined AO-SLO-OCT system.

5. Conclusion

We have presented here our latest progress on the development of a multi-modal *in vivo* mouse retina imaging system. The current instrument includes the addition and integration of an OCT into our previously built AO-SLO system to create an AO-SLO-OCT instrument. The system design, performance, and example images were presented. Several important points observed during the system development were discussed as well. First, by using a pair of axicon lenses to generate a Bessel beam to act as the AO beacon, one can improve the robustness of AO by extending the depth of focus without a reduction of beam power or reference spot size. However, AO performance was sensitive to the alignment of the axicon pair because of the extra aberrations, probably caused by some back-reflected rather than backscattered light reaching the wavefront sensor. This effect should be studied in more detail. Second, integrating an OCT into an existing system using the reflection by the dichroic mirror can be problematic if the broadband OCT spectrum is of interest. This is due to the group delay dispersion introduced by the reflection by a dichroic mirror, suggesting it is preferred to integrate OCT into a multi-modal system using a dichroic in the transmission path. Third, while our multi-modal mouse retinal imaging system

was built to operate two imaging modalities simultaneously, due to the limited imaging speed of the OCT engine (200kHz), it was not possible to reliably correct motion artifacts and co-register the serial AO-SLO images and AO-OCT volumes at this acquisition speed. This is because of the small FOV of the mouse retina imaged (~10× smaller than in the human eye). Any eye movements were greatly amplified. In order to obtain the AO-OCT volumes with only modest eye motion artifacts, which could be corrected in postprocessing, a high-speed OCT engine is necessary.

Funding. National Science Foundation (I/UCRC CBSS Grant); National Eye Institute (EY012576, EY026556, EY02660, EY031098); Dalian University of Technology (DUT21RC(3)001, DUT21YG121); National Natural Science Foundation of China (62175024); Canadian Institutes of Health Research.

Acknowledgments. We want to acknowledge the generous contribution of prof. Edward N. Pugh, Jr, and support of dr. Suman Manna from UCD EyePod. The help of Dr. Yifan Jian from OHSU is greatly appreciated as well.

Disclosures. The authors declare that there are no conflicts of interest.

Data availability. Data underlying the results presented in this paper are not publicly available but may be obtained from the authors upon reasonable request.

Supplemental document. See [Supplement 1](#) for supporting content.

References

1. R. H. Webb and G. W. Hughes, "Scanning laser ophthalmoscope," *IEEE Trans. Biomed. Eng.* **BME-28**(7), 488–492 (1981).
2. M. W. Seeliger, S. C. Beck, N. Pereyra-Munoz, S. Dangel, J. Y. Tsai, U. F. O. Luhmann, S. A. van de Pavert, J. Wijnholds, M. Samardzija, A. Wenzel, E. Zrenner, K. Narfstrom, E. Fahl, N. Tanimoto, N. Acar, and F. Tonagel, "In vivo confocal imaging of the retina in animal models using scanning laser ophthalmoscopy," *Vision Res.* **45**(28), 3512–3519 (2005).
3. M. Paques, M. Sironnutti, M. J. Roux, S. Picaud, E. Levavasseur, C. Bellman, and J. A. Sahel, "High resolution fundus imaging by confocal scanning laser ophthalmoscopy in the mouse," *Vision Res.* **46**(8-9), 1336–1345 (2006).
4. D. Huang, E. Swanson, C. Lin, J. Schuman, W. Stinson, W. Chang, M. Hee, T. Flotte, K. Gregory, and C. Puliafito, "Optical coherence tomography," *Science* **254**(5035), 1178–1181 (1991).
5. W. Drexler, U. Morgner, R. K. Ghanta, F. X. Kärtner, J. S. Schuman, and J. G. Fujimoto, "Ultrahigh-resolution ophthalmic optical coherence tomography," *Nat. Med.* **7**(4), 502–507 (2001).
6. R. Leitgeb, C. K. Hitzenberger, and A. F. Fercher, "Performance of fourier domain vs. time domain optical coherence tomography," *Opt. Express* **11**(8), 889–894 (2003).
7. J. G. Fujimoto, "Optical coherence tomography for ultrahigh resolution in vivo imaging," *Nat. Biotechnol.* **21**(11), 1361–1367 (2003).
8. W. Drexler and J. G. Fujimoto, "State-of-the-art retinal optical coherence tomography," *Prog. Retinal Eye Res.* **27**(1), 45–88 (2008).
9. E. S. Levine, A. Zam, P. Zhang, A. Pechko, X. Wang, P. FitzGerald, E. N. Pugh, R. J. Zawadzki, and M. E. Burns, "Rapid light-induced activation of retinal microglia in mice lacking Arrestin-1," *Vision Res.* **102**, 71–79 (2014).
10. P. Zhang, A. Zam, Y. Jian, X. Wang, Y. Li, K. Lam, M. E. Burns, M. V. Sarunic, E. N. Pugh, and R. J. Zawadzki, "In vivo wide-field multispectral scanning laser ophthalmoscopy-optical coherence tomography mouse retinal imager: longitudinal imaging of ganglion cells, microglia, and Muller glia, and mapping of the mouse retinal and choroidal vasculature," *J. Biomed. Opt.* **20**(12), 126005 (2015).
11. P. Zhang, M. Goswami, R. J. Zawadzki, and J. E. N. Pugh, "The photosensitivity of rhodopsin bleaching and light-induced increases of fundus reflectance in mice measured in vivo with scanning laser ophthalmoscopy," *Invest. Ophthalmol. Visual Sci.* **57**(8), 3650–3664 (2016).
12. P. Zhang, R. J. Zawadzki, M. Goswami, P. T. Nguyen, V. Yarov-Yarovoy, M. E. Burns, and E. N. Pugh, "In vivo optophysiology reveals that G-protein activation triggers osmotic swelling and increased light scattering of rod photoreceptors," *Proc. Natl. Acad. Sci.* (2017).
13. P. Zhang, E. B. Miller, S. K. Manna, R. K. Meleppat, E. N. Pugh Jr., and R. J. Zawadzki, "Temporal speckle-averaging of optical coherence tomography volumes for in-vivo cellular resolution neuronal and vascular retinal imaging," *Neurophotonics* **6**(04), 1 (2019).
14. C. K. Brinkmann, S. Wolf, and U. E. K. Wolf-Schnurrbusch, "Multi-modal imaging in macular diagnostics: combined OCT-SLO improves therapeutical monitoring," *Graefe's Arch. Clin. Exp. Ophthalmol.* **246**(1), 9–16 (2007).
15. P. Charbel Issa, R. P. Finger, F. G. Holz, and H. P. N. Scholl, "Multimodal imaging including spectral domain oct and confocal near infrared reflectance for characterization of outer retinal pathology in pseudoxanthoma elasticum," *Invest. Ophthalmol. Visual Sci.* **50**(12), 5913–5918 (2009).
16. S. Wei, W. Qing, L. Tan, K. David, F. Z. Hao, M. B. Janice, and J. Shuliang, "Integrating photoacoustic ophthalmoscopy with scanning laser ophthalmoscopy, optical coherence tomography, and fluorescein angiography for a multi-modal retinal imaging platform," *J. Biomed. Opt.* **17**(6), 061206 (2012).

17. J. D. Malone, M. T. El-Haddad, I. Bozic, L. A. Tye, L. Majeau, N. Godbout, A. M. Rollins, C. Boudoux, K. M. Joos, S. N. Patel, and Y. K. Tao, "Simultaneous multi-modal ophthalmic imaging using swept-source spectrally encoded scanning laser ophthalmoscopy and optical coherence tomography," *Biomed. Opt. Express* **8**(1), 193–206 (2017).
18. R. Almasi, A. Vafaei, Z. Ghasemi, M. R. Ommani, A. R. Dehghani, and H. Rabbani, "Registration of fluorescein angiography and optical coherence tomography images of curved retina via scanning laser ophthalmoscopy photographs," *Biomed. Opt. Express* **11**(7), 3455–3476 (2020).
19. Y. Zhang and A. Roorda, "Evaluating the lateral resolution of the adaptive optics scanning laser ophthalmoscope," *J. Biomed. Opt.* **11**(1), 014002 (2006).
20. P. Zhang, M. Goswami, A. Zam, E. N. Pugh, and R. J. Zawadzki, "Effect of scanning beam size on the lateral resolution of mouse retinal imaging with SLO," *Opt. Lett.* **40**(24), 5830–5833 (2015).
21. R. Trikha, L. S. Morse, R. J. Zawadzki, J. S. Werner, and S. S. Park, "Ten-year follow-up of eyes treated with stereotactic fractionated external beam radiation for neovascular age-related macular degeneration," *Retina* **31**(7), 1303–1315 (2011).
22. Y. Geng, A. Dubra, L. Yin, W. H. Merigan, R. Sharma, R. T. Libby, and D. R. Williams, "Adaptive optics retinal imaging in the living mouse eye," *Biomed. Opt. Express* **3**(4), 715–734 (2012).
23. S. Bonora, Y. F. Jian, P. F. Zhang, A. Zam, E. N. Pugh, R. J. Zawadzki, and M. V. Sarunic, "Wavefront correction and high-resolution in vivo OCT imaging with an objective integrated multi-actuator adaptive lens," *Opt. Express* **23**(17), 21931–21941 (2015).
24. E. A. Rossi, C. E. Granger, R. Sharma, Q. Yang, K. Saito, C. Schwarz, S. Walters, K. Nozato, J. Zhang, T. Kawakami, W. Fischer, L. R. Latchney, J. J. Hunter, M. M. Chung, and D. R. Williams, "Imaging individual neurons in the retinal ganglion cell layer of the living eye," *Proc. Natl. Acad. Sci.* **114**(3), 586–591 (2017).
25. Z. Liu, K. Kurokawa, F. Zhang, J. J. Lee, and D. T. Miller, "Imaging and quantifying ganglion cells and other transparent neurons in the living human retina," *Proc. Natl. Acad. Sci.* **114**(48), 12803–12808 (2017).
26. M. Mujat, R. D. Ferguson, A. H. Patel, N. Ifimia, N. Lue, and D. X. Hammer, "High resolution multi-modal clinical ophthalmic imaging system," *Opt. Express* **18**(11), 11607–11621 (2010).
27. R. J. Zawadzki, S. M. Jones, S. Pilli, S. Balderas-Mata, D. Y. Kim, S. S. Olivier, and J. S. Werner, "Integrated adaptive optics optical coherence tomography and adaptive optics scanning laser ophthalmoscope system for simultaneous cellular resolution in vivo retinal imaging," *Biomed. Opt. Express* **2**(6), 1674–1686 (2011).
28. D. X. Hammer, R. Daniel Ferguson, M. Mujat, A. Patel, E. Plumb, N. Ifimia, T. Y. P. Chui, J. D. Akula, and A. B. Fulton, "Multi-modal adaptive optics retinal imager: design and performance," *J. Opt. Soc. Am. A* **29**(12), 2598–2607 (2012).
29. Z. Liu, J. Tam, O. Saeedi, and D. X. Hammer, "Trans-retinal cellular imaging with multi-modal adaptive optics," *Biomed. Opt. Express* **9**(9), 4246–4262 (2018).
30. Z. Liu, F. Zhang, K. Zucca, A. Agrawal, and D. X. Hammer, "Ultrahigh-speed multi-modal adaptive optics system for microscopic structural and functional imaging of the human retina," *Biomed. Opt. Express* **13**(11), 5860–5878 (2022).
31. A. J. Bower, T. Liu, N. Aguilera, J. Li, J. Liu, R. Lu, J. P. Giannini, L. A. Huryn, A. Dubra, Z. Liu, D. X. Hammer, and J. Tam, "Integrating adaptive optics-SLO and OCT for multi-modal visualization of the human retinal pigment epithelial mosaic," *Biomed. Opt. Express* **12**(3), 1449–1466 (2021).
32. G. Palczewska, P. Stremplewski, S. Suh, N. Alexander, D. Salom, Z. Dong, D. Ruminski, E. H. Choi, A. E. Sears, T. S. Kern, M. Wojtkowski, and K. Palczewski, "Two-photon imaging of the mammalian retina with ultrafast pulsing laser," *JCI Insight* **3**(17), (2018).
33. D. J. Wahl, M. J. Ju, Y. Jian, and M. V. Sarunic, "Non-invasive cellular-resolution retinal imaging with two-photon excited fluorescence," *Biomed. Opt. Express* **10**(9), 4859–4873 (2019).
34. Z. Qin, S. He, C. Yang, J. S. Yung, C. Chen, C. K. Leung, K. Liu, and J. Y. Qu, "Adaptive optics two-photon microscopy enables near-diffraction-limited and functional retinal imaging in vivo," *Light: Sci. Appl.* **9**(1), 79 (2020).
35. R. J. Zawadzki, P. Zhang, A. Zam, E. B. Miller, M. Goswami, X. Wang, R. S. Jonnal, S.-H. Lee, D. Y. Kim, J. G. Flannery, J. S. Werner, M. E. Burns, and E. N. Pugh, "Adaptive-optics SLO imaging combined with widefield OCT and SLO enables precise 3D localization of fluorescent cells in the mouse retina," *Biomed. Opt. Express* **6**(6), 2191–2210 (2015).
36. J. Mocchi, M. Quintavalla, C. Trestino, S. Bonora, and R. Muradore, "A multi-platform CPU-based architecture for cost-effective adaptive optics systems," *IEEE Transactions on Industrial Informatics* **PP** 1 (2018).
37. Y. Geng, L. A. Schery, R. Sharma, A. Dubra, K. Ahmad, R. T. Libby, and D. R. Williams, "Optical properties of the mouse eye," *Biomed. Opt. Express* **2**(4), 717–738 (2011).
38. P. Zhang, J. Mocchi, D. J. Wahl, R. K. Meleppat, S. K. Manna, M. Quintavalla, R. Muradore, M. V. Sarunic, S. Bonora, E. N. Pugh Jr., and R. J. Zawadzki, "Effect of a contact lens on mouse retinal in vivo imaging: Effective focal length changes and monochromatic aberrations," *Exp. Eye Res.* **172**, 86–93 (2018).
39. D. J. Wahl, P. Zhang, J. Mocchi, M. Quintavalla, R. Muradore, Y. Jian, S. Bonora, M. V. Sarunic, and R. J. Zawadzki, "Adaptive optics in the mouse eye: wavefront sensing based vs. image-guided aberration correction," *Biomed. Opt. Express* **10**(9), 4757–4774 (2019).
40. E. B. Miller, P. Zhang, K. Ching, E. N. Pugh Jr., and M. E. Burns, "In vivo imaging reveals transient microglia recruitment and functional recovery of photoreceptor signaling after injury," *Proc. Natl. Acad. Sci. U.S.A.* **116**(33), 16603–16612 (2019).

41. C.-J. Jeon, E. Strettoi, and R. H. Masland, "The major cell populations of the mouse retina," *J. Neurosci.* **18**(21), 8936–8946 (1998).
42. X. Yao, R. Lu, B. Wang, Y. Lu, and T.-H. Kim, "Super-resolution ophthalmoscopy: Virtually structured detection for resolution improvement in retinal imaging," *Exp. Biol. Med.* **246**(3), 249–259 (2021).
43. L. D. Carter-Dawson and M. M. Lavail, "Rods and cones in the mouse retina. I. Structural analysis using light and electron microscopy," *J. Comp. Neurol.* **188**(2), 245–262 (1979).
44. X. Zhou, P. Bedggood, and A. Metha, "Limitations to adaptive optics image quality in rodent eyes," *Biomed. Opt. Express* **3**(8), 1811–1824 (2012).
45. M. Pircher, E. Götzinger, and C. K. Hitzenberger, "Dynamic focus in optical coherence tomography for retinal imaging," *J. Biomed. Opt.* **11**(5), 054013 (2006).
46. M. Wojtkowski, V. J. Srinivasan, T. H. Ko, J. G. Fujimoto, A. Kowalczyk, and J. S. Duker, "Ultrahigh-resolution, high-speed, Fourier domain optical coherence tomography and methods for dispersion compensation," *Opt. Express* **12**(11), 2404–2422 (2004).
47. J. B. Guild, C. Xu, and W. W. Webb, "Measurement of group delay dispersion of high numerical aperture objective lenses using two-photon excited fluorescence," *Appl. Opt.* **36**(1), 397–401 (1997).
48. R. J. Zawadzki, B. Cense, Y. Zhang, S. S. Choi, D. T. Miller, and J. S. Werner, "Ultrahigh-resolution optical coherence tomography with monochromatic and chromatic aberration correction," *Opt. Express* **16**(11), 8126–8143 (2008).
49. Y. F. Jian, J. Xu, M. A. Gradowski, S. Bonora, R. J. Zawadzki, and M. V. Sarunic, "Wavefront sensorless adaptive optics optical coherence tomography for in vivo retinal imaging in mice," *Biomed. Opt. Express* **5**(2), 547–559 (2014).
50. D. J. Wahl, Y. Jian, S. Bonora, R. J. Zawadzki, and M. V. Sarunic, "Wavefront sensorless adaptive optics fluorescence biomicroscope for in vivo retinal imaging in mice," *Biomed. Opt. Express* **7**(1), 1–12 (2016).
51. J. P. Giannini, R. Lu, A. J. Bower, R. Fariss, and J. Tam, "Visualizing retinal cells with adaptive optics imaging modalities using a translational imaging framework," *Biomed. Opt. Express* **13**(5), 3042–3055 (2022).
52. S. Omri, B. Omri, M. Savoldelli, L. Jonet, B. Thillaye-Goldenberg, G. Thuret, P. Gain, J. C. Jeanny, P. Crisanti, and F. Behar-Cohen, "The outer limiting membrane (OLM) revisited: clinical implications," *Clin Ophthalmol* **4**, 183–195 (2010).
53. P. Zhang, S. K. Manna, E. B. Miller, Y. Jian, R. K. Meleppat, M. V. Sarunic, E. N. Pugh Jr., and R. J. Zawadzki, "Aperture phase modulation with adaptive optics: a novel approach for speckle reduction and structure extraction in optical coherence tomography," *Biomed. Opt. Express* **10**(2), 552–570 (2019).